Journal of Computational Physics 401 (2020) 109027

Contents lists available at ScienceDirect

Journal of Computational Physics

www.elsevier.com/locate/jcp

# Distributed current source modeling method for 3D eddy current problem in magnetic conductor with discrete state-space **J**-$\varphi$ formulation

Bingjie Hao [a], Kok-Meng Lee [a,b,*], Kun Bai [a,*]

[a] State Key Lab of Digi. Manuf. Equip. and Tech., Huazhong Univ. of Sci. and Tech., Wuhan 430074, China
[b] Woodruff Sch. of Mech. Eng., Georgia Inst. of Tech., Atlanta, GA 30332, USA

ARTICLE INFO

*Article history:*
Received 15 February 2019
Received in revised form 21 August 2019
Accepted 12 October 2019
Available online 17 October 2019

*Keywords:*
Eddy current
Magnetic material
State space model
Current sources

ABSTRACT

This paper presents a distributed-current-source (DCS) modeling method to analyze the eddy-current (EC) induced in an electrically conductive material with a weak magnetic permeability. Formulated in state space to solve for an unknown EC density **J** and electric potential $\varphi$, the method decomposes the conductor into elemental volume/surface current sources to model the eddy-current and magnetization effects. The closed-form solutions to a three-dimension (3D) EC problem with geometrical boundary effects are derived and verified by comparing with finite-element methods and published data, both numerically and experimentally. An element-refinement method, which accounts for the skin-depth effects and non-uniform boundary EC, is proposed and validated. The DCS modeling method has been applied to a field-reconstruction application for parametric analysis demonstrating its effectiveness and efficiency.



## 1. Introduction

Eddy current (EC) effect is a useful phenomenon that has been applied to various fields ranging from industrial applications including geometrical and material sensing [1], induction heating [2] and vibration damping to emerging medical applications like magnetic induction tomography [3] and transcranial magnetic stimulation [4] to name a few. Eddy current models are important analyzing tools for sensor design optimization, damping force analysis, energy loss prediction in electromagnetic devices and EC visualization in defect detection and field reconstruction [5].

EC is often seen in conductive metal induced by an electromagnet (EM) powered by a time-varying current. As a typical PDE problem, various modeling methods have been studied in the past few decades. Analytical solutions [6] and improved TREE model [7], which were generally derived for axisymmetric systems, are the most well-known methods as they can be employed to fast computing. These axisymmetric models, however, assume that eddy currents are circumferential and planar, and solve for the only unknown magnetic vector potential (MVP) **A** with the Coulomb gauge, from which the magnetic flux density (MFD) **B** and eddy current density (ECD) **J** are derived. For a more general 3D EC system where the conductor has complicated shapes, analytical solutions have difficulties handling the boundary conditions. These problems are often solved numerically using techniques like finite element analysis (FEA) [8–16], finite volume method [17] and finite difference method [18]. Among them, FEA has been a most popular solving tool for 3D EC problems because commercial software

* Corresponding authors.
*E-mail address:* kokmeng.lee@me.gatech.edu (K.-M. Lee).

https://doi.org/10.1016/j.jcp.2019.109027
0021-9991/

packages are widely available. FEA methods solve the approximate PDE solutions with appropriate boundary constraints in each of the discretized elements, and use nodes [15] or edges [9,16] to establish shape functions; the latter is believed to yield better accuracies when modeling the media interface where the electric and/or magnetic fields may be spatially discontinuous. Since the MVP alone is not sufficient to describe the electromagnetic field, two kinds of formulations are widely used; **A**-$\varphi$ formulation [3,10,11] that solves for the magnetic vector potential and electric scalar potential, and **T**-$\Omega$ formulation [12–14] that treats electric vector potential **T** and magnetic scalar potential $\Omega$ as unknown. The **T**-$\Omega$ formulation has the advantage of decreasing the unknowns in nonconductor region, thus has gained greater adoption in recent years. Regardless the kinds of potential functions or element types in the numerical formulation, FEA requires modeling a sufficiently large non-conducting region (including air space) consequently demanding much more degrees of freedom and causing convergence issues, which must be carefully handled.

Inspired by the fact that the MVP and MFD fields can be viewed as the effects of current sources, a method called distributed current source (DCS) model [19] that decomposes the conductor into elemental current-sources as distributed-state-variables was developed for solving EC induced in non-magnetic conductors. Since eddy-currents only exist in conducting regions, element discretization is not required in airspace; thus, the DCS model dramatically decreases the number of unknowns. The governing equation for EC system can be derived by considering the mutual induction between current sources, which can be assembled in state-space representation [20] that familiar to workers in the field of control engineering. Well established methods for solving the dynamic responses can be used to solve EC problems in both time and frequency domains. The ECD **J** induced by a time-varying magnetic field was solved using the DCS method for a large conductive plate without boundaries, generally for nonmagnetic conductors. In [20], the ECD was solved as a constrained least-square problem neglecting the electric potential effects. Different from existing models that have been widely studied for non-magnetic conductors, models for magnetic materials are more complicated because the magnetization effects alter the ECD and MFD distributions. Magnetic materials can be characterized by a permeability that covers a wide range of values. Materials like austenitic stainless steels and metal alloy [21,22] may have a weak permeability commonly seen in manufacturing applications. For example, austenitic stainless steels, such as AISI 304, 316L are widely used in additive manufacturing. Phase transformations from austenite to martensite may happen during the manufacturing process weakly magnetizing the otherwise nonmagnetic conductor, which could affect the final mechanical property [23].

Motivated by the fact that EC-effects have potential applications in monitoring additive manufacturing processes, this paper focuses on extending the EC models to account for the presence of weak permeability in materials with linear magnetic properties, where saturation and hysteresis effects can be neglected. Specifically, this paper improves the DCS modeling method by accounting for the electric potential and the magnetization effects in the formulation, and thus extends the scope of EC applications. The remainder of the paper offers the following:

- The DCS model introduces equivalent magnetizing currents to account for the magnetization effect in the (**J**-$\varphi$) state-space formulation where both the ECD **J** and Electric potential $\varphi$ are treated as unknown variables. Next, the discrete-time domain solutions allowing for arbitrary inputs and closed-form harmonic solutions are derived, which solve both the ECD and electric potential simultaneously. As will be shown, the optimal problem for solving ECD [20] can be reduced to solving a compact and yet physically intuitive set of linear equations.
- Along a proposed procedure for optimizing the element sizes, the DCS modeled harmonic and time-domain solutions involving boundary and magnetization effects are illustrated numerically and experimentally. The computing accuracy of the 2D and 3D solutions are validated by comparing with finite-element methods and published data.
- The advantage and computing-efficiency of the DCS modeling method are illustrated in the context of a practical field reconstruction application. As will be shown, the method is more efficient than conventional FEA methods in solving EC problems involving conductors with non-conductive elements.

## 2. Method

Fig. 1(a) shows a typical eddy-current system where the time-varying magnetic field generated by the electromagnet (EM) coil not only induces an ECD field in the magnetic conductor but also magnetizes its material. The operating condition is assumed magneto quasi-static for a relatively low frequency ($f \leq 1$ MHz) applications where the displacement current can be ignored. The electric field intensity **E**, time-varying magnetic flux density **B** and magnetic field intensity **H** are given by the Maxwell-Faraday equation and Ampère's law (1a, b):

$$\nabla \times \mathbf{E} = -\frac{\partial \mathbf{B}}{\partial t}, \tag{1a}$$

$$\nabla \times \mathbf{H} = \mathbf{J} + \mathbf{J}_e. \tag{1b}$$

In (1b), **J** is the ECD induced in the conductor by the magnetic field; and $\mathbf{J}_e$ is the current density in the EM coil through which the current $u$ flows. The ECD **J** induced in the conductor obeys Ohm's law (2a) where $\sigma$ is the electrical conductivity. For a linear magnetic material, **B** and **H** are related by the constitutive relationship in (2b) where the vector **M** represents the volume density of the magnetic moment due to the material magnetization by **H**, $\mu_0$ is the permeability of free space and $\mu_r$ is relative magnetic permeability:

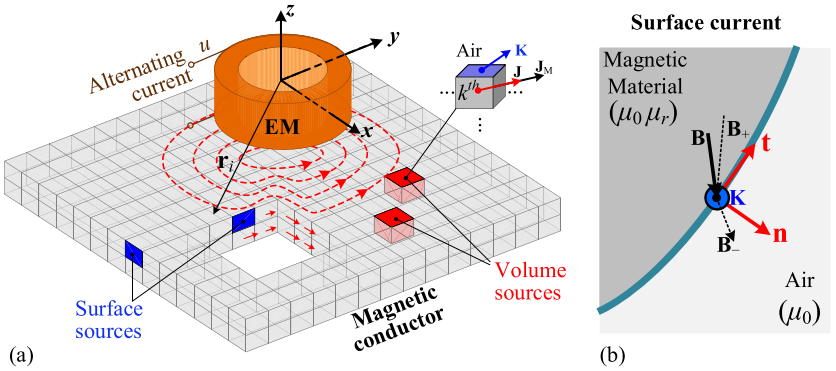


**Fig. 1.** Schematics of EM/Conductor system. (a) Conductor with distributed current source modeling. (b) Illustration of surface current density.

$$\mathbf{J} = \sigma \mathbf{E}; \tag{2a}$$

$$\mathbf{B} = \mu_0(\mathbf{H} + \mathbf{M}) = \mu_0 \mu_r \mathbf{H}. \tag{2b}$$

Since the eddy current flows into any volume of space equal to that flows out but cannot flow into non-conductive material, it satisfies the continuity equation (3a) and the boundary condition (3b) where $\mathbf{n}$ is the normal vector out of conductor boundary:

$$\nabla \cdot \mathbf{J} = 0; \tag{3a}$$

$$\mathbf{J} \cdot \mathbf{n} = 0. \tag{3b}$$

Equations (1a, b), (2a, b) and (3a), along with the boundary condition (3b), provide a basis to solve for the ECD $\mathbf{J}$ induced in the conductor. However, the solutions to $\mathbf{J}$ for a given current input $u$ involve solving $\mathbf{M}$ in the conductor and $\mathbf{B}$ in the total space (including the EM and free space). Alternatively, the 3D eddy-current boundary-value problem can be recast in state space using DCS modeling method, which converts the boundary value problem into an initial value problem directly solving $\mathbf{J}$ for a given current input $u$ as derived in Subsection 2.1.

### *2.1. Discrete state-space $\mathbf{J}$-$\varphi$ formulation using DCS models*

In the DCS modeling method, the magnetization $\mathbf{M}$ in the conductor is equivalently modeled [19] as a pair of volume current density $\mathbf{J}_\mathrm{M}$ and surface current density $\mathbf{K}$:

$$\mathbf{J}_\mathrm{M} = \nabla \times \mathbf{M} \quad \text{and} \tag{4a}$$

$$\mathbf{K} = \mathbf{M} \times \mathbf{n}. \tag{4b}$$

Inside the conductor, $\mathbf{J}_e$ is zero and $\mathbf{M} = (\mu_r - 1)\mathbf{H}$ from (2b). From (1b) and (4a), the total volume current density $\mathbf{J}_\mathrm{T}$ inside the conductor can thus be expressed as

$$\mathbf{J}_\mathrm{T} = \mathbf{J} + \mathbf{J}_\mathrm{M} = \mu_r \mathbf{J}. \tag{5}$$

As derived in Appendix with the aid of Fig. 1(b), the surface magnetizing current density $\mathbf{K}$ (4b) is a function of the external magnetic flux density $\mathbf{B}$ at the conductor/air inference:

$$\mathbf{K} = \rho \mathbf{B} \times \mathbf{n} \quad \text{where } \rho = \frac{2}{\mu_0} \frac{\mu_r - 1}{\mu_r + 1}. \tag{6}$$

With (5) and (6), the eddy-current and magnetization effects are modeled as current sources in the governing equation for solving $\mathbf{J}$, which can be derived from (1a) and (2a) where $\mathbf{J}$ is replaced by $\mathbf{J}_\mathrm{T}$ (5). Noting that $\nabla \times (-\nabla\varphi) = 0$ where $\varphi$ is a scalar electric potential, $\mathbf{J}$ can be expressed in terms of a magnetic vector potential $\mathbf{A}$ (where $\mathbf{B} = \nabla \times \mathbf{A}$ and $\nabla \cdot \mathbf{A} = 0$):

$$\mathbf{J} = -\sigma \frac{\partial \mathbf{A}}{\partial t} - \sigma \nabla \varphi. \tag{7}$$

In the right side of (7), the 1st term represents the ECD generated by the time-varying magnetic fields contributed by the current sources ($\mathbf{J}_e$, $\mathbf{J}_\mathrm{T}$ and $\mathbf{K}$); and the 2nd term accounts for the charge accumulation. Along with the continuity equation (3a) and the boundary condition (3b), $\mathbf{J}$ is the solutions to the $\mathbf{J}$-$\varphi$ equation (7) where $\varphi$ is treated as additional unknown. For an axisymmetric system, $\mathbf{J}$ (and hence $\mathbf{A}$) has only a non-zero component in the circumferential ($\phi$) direction and

$\partial\varphi/\partial\phi = 0$ due to symmetry, which imply $\nabla\varphi = 0$, the 2nd term vanishes in (7), and the corresponding constraints (3a, b) are automatically satisfied. In general, $\varphi$ may not be a constant and its gradient $\nabla\varphi$ could have an influence on the ECD distribution especially near the boundaries; the corresponding constraints of $\mathbf{J}$ cannot be automatically satisfied and must be explicitly accounted for.

*2.1.1. Derivation of discrete state-space system equation*

The DCS method decomposes the conductor into $n$ elemental-volume sources and $m$ elemental-surface sources. As shown in (8) where the components are defined in (9a-c), the MVP in the $i$th volume, $\mathbf{A}_i$, is contributed by $\mathbf{A_e}$ due to the time-varying magnetic field generated by the input current $u$ flowing through the EM, and ($\mathbf{A_v}$, $\mathbf{A_b}$) of the volume and surface current sources of the conductor:

$$\mathbf{A}_i = \mathbf{A_e}i + \sum_{l=1}^{n} \mathbf{A_v}il + \sum_{k=1}^{m} \mathbf{A_b}ik \tag{8}$$

$$\mathbf{A_e}i = \mathbf{f_e}(\mathbf{r}_i)u, \quad \text{where } \mathbf{f_e}(\mathbf{r}_i) = \frac{\mu_0 C_0}{4\pi} \int_{V_E} \frac{\mathbf{e}_\theta}{r_i} d\upsilon \text{ and } r_i = |\mathbf{r}_i - \mathbf{r}|; \tag{9a}$$

$$\frac{\mathbf{A_v}il}{\mu_r \nu_l} = f_{\mathrm{v}}(r_{il})\mathbf{J}_l, \quad \text{where } f_{\mathrm{v}}(r_{il}) = \frac{\mu_0}{4\pi\, \nu_i \nu_l} \int_{\nu_i} \int_{\nu_l} \frac{d\upsilon}{r_{il}} d\upsilon \tag{9b}$$

$$\text{and} \quad \frac{\mathbf{A_b}ik}{s_k} = f_{\mathrm{b}}(r_{ik})\mathbf{K}_k, \quad \text{where } f_{\mathrm{b}}(r_{ik}) = \frac{\mu_0}{4\pi\, \nu_i s_k} \int_{\nu_i} \int_{s_k} \frac{ds}{r_{ik}} d\upsilon. \tag{9c}$$

In (9a-c), $d\upsilon$ and $ds$ denote the differential volume and surface respectively; $V_E$ is the volume of EM; and ($\nu_{\mathrm{i}}$ and $s_k$) denote the ($i$th volume and $k$th surface-area). In (9a), $\mathbf{A_e}$ at the location $\mathbf{r}_i = [x_i \;\; y_i \;\; z_i]^{\mathrm{T}}$, which is linear with respect to the input current $u$, can be computed from the integral solution to the vector Poisson's equation [24]. The proportionality between $\mathbf{A_e}$ and $u$ is expressed as a kernel (vector) function $\mathbf{f_e}$ where $C_0$ is the current density with unit current (1 Ampere) flowing through the coil wire; and the vectors in the integral over the coil, $\mathbf{r}$ and $\mathbf{e}_\theta$, denote the position of the target element and unit-direction of the current respectively. Similarly, $\mathbf{A_v}$ and $\mathbf{A_b}$ can be computed with a pair of kernel (scalar) functions as shown in (9b, c). The integral ($f_{\mathrm{v}}$ or $f_{\mathrm{b}}$) accounts for the average effects of the mutual induction between a target $\nu_i$ element and a source element ($\nu_l$ or $s_k$ with unit current density). However, $f_{\mathrm{v}}$ and $f_{\mathrm{b}}$ involve double integrals and their computations, though straightforward, are time-consuming. For sufficiently small elements, the elements can be treated as point sources and thus, both the scalar kernels ($f_{\mathrm{v}}$ and $f_{\mathrm{b}}$) between the source element at $\mathbf{r}_j$ and the target element at $\mathbf{r}_i$ can be approximated by (10):

$$f_{(\mathrm{v,b})}(r_{ij}) \approx \frac{\mu_0}{4\pi} \begin{cases} 1/r_{ij} & r_{ij} \neq 0 \\ 2/(3b_j) & r_{ij} = 0 \end{cases} \tag{10}$$

where $b$ is the radius of a minimum bounding circle (or sphere) that enclose the surface or volume element [19].

With equation (7) and the elemental MVP in (8), the discretized EC system can be compactly represented in matrix form:

$$\frac{\mathbf{J}}{-\sigma} = \mu_r \mathbf{F}_1 \frac{\partial \mathbf{J}}{\partial t} + \mathbf{F}_2 \frac{\partial \mathbf{K}}{\partial t} + \boldsymbol{\Gamma}\boldsymbol{\Phi} + \mathbf{h}_1 \dot{u} \tag{11}$$

where $\mathbf{J}(\in \mathbb{R}^{3n\times 1}) = [\mathbf{J}_1^{\mathrm{T}} \cdots \mathbf{J}_i^{\mathrm{T}} \cdots \mathbf{J}_n^{\mathrm{T}}]^{\mathrm{T}}$; $\mathbf{J}_i = [J_{ix} \;\; J_{iy} \;\; J_{iz}]^{\mathrm{T}}$;

$$\mathbf{K}\left(\in \mathbb{R}^{3m\times 1}\right) = \left[\mathbf{K}_1^{\mathrm{T}} \cdots \mathbf{K}_k^{\mathrm{T}} \cdots \mathbf{K}_m^{\mathrm{T}}\right]^{\mathrm{T}}; \; \mathbf{K}_k = [K_{kx} \; K_{ky} \; K_{kz}]^{\mathrm{T}};$$

and $\boldsymbol{\Phi}(\in \mathbb{R}^{n\times 1}) = [\varphi_1 \cdots \varphi_i \cdots \varphi_n]^{\mathrm{T}}$. In (11), $\boldsymbol{\Gamma}(\in \mathbb{R}^{3n\times n})$ is the gradient operation matrix; and $\mathbf{h}_1$, $\mathbf{F}_1$ and $\mathbf{F}_2$ associated with the kernel functions (9a-c), are defined as

$$\mathbf{h}_1\left(\in \mathbb{R}^{3n\times 1}\right) = [\,\mathbf{f_e}^{\mathrm{T}}(\mathbf{r}_1) \cdots \;\; \mathbf{f_e}^{\mathrm{T}}(\mathbf{r}_i) \cdots \;\; \mathbf{f_e}^{\mathrm{T}}(\mathbf{r}_n)\,]^{\mathrm{T}}$$

$$\mathbf{F}_1\left(\in \mathbb{R}^{3n\times 3n}\right) = \begin{bmatrix} \nu_1\mathbf{f_v}(r_{11}) \cdots & \nu_l\mathbf{f_v}(r_{1l}) \cdots & \nu_n\mathbf{f_v}(r_{1n}) \\ \vdots \cdots & \vdots \cdots & \vdots \\ \nu_1\mathbf{f_v}(r_{n1}) \cdots & \nu_l\mathbf{f_v}(r_{nl}) \cdots & \nu_n\mathbf{f_v}(r_{nn}) \end{bmatrix};$$

$$\text{and} \quad \mathbf{F}_2\left(\in \mathbb{R}^{3n\times 3m}\right) = \begin{bmatrix} s_1\mathbf{f_b}(r_{11}) \cdots & s_k\mathbf{f_b}(r_{1k}) \cdots & s_m\mathbf{f_b}(r_{1m}) \\ \vdots \cdots & \vdots \cdots & \vdots \\ s_1\mathbf{f_b}(r_{n1}) \cdots & s_k\mathbf{f_b}(r_{nk}) \cdots & s_m\mathbf{f_b}(r_{nm}) \end{bmatrix};$$

where the kernel vectors ($\mathbf{f_v}, \mathbf{f_b}$) are diagonal matrix, $\mathbf{f}_{(\mathbf{v},\mathbf{b})}(r_{ij}) = f_{(\mathrm{v,b})}(r_{ij})\mathbf{I}_3$ and $\mathbf{I}_3$ is a $3 \times 3$ identity matrix.

For the $k$th surface element, (6) can be rewritten as

$$\mathbf{K}_k = \rho \mathbf{B}_k \times \mathbf{n}_k \quad \text{or} \quad \mathbf{K}_k = -\rho [\mathbf{n}_k]_\times \mathbf{B}_k \tag{12}$$

where $[\mathbf{n}_k]_\times$ denotes the skew matrix of vector $\mathbf{n}_k$, that is,

$$[\mathbf{n}_k]_\times = \begin{bmatrix} 0 & -n_{kz} & n_{ky} \\ n_{kz} & 0 & -n_{kx} \\ -n_{ky} & n_{kx} & 0 \end{bmatrix}.$$

As in (8) and (9a-c), $\mathbf{B_k}$ in (12), is contributed by the time-varying magnetic fields $\mathbf{B_e}$ of the EM, and ($\mathbf{B_v}$, $\mathbf{B_b}$) of the volume and current sources of the conductor:

$$\mathbf{B}_k = \mathbf{B}_{\mathbf{e}k} + \sum_{l=1}^{n} \mathbf{B}_{\mathbf{v}kl} + \sum_{i=1}^{m} \mathbf{B}_{\mathbf{b}ki} \tag{13}$$

$$\mathbf{B}_{\mathbf{e}k} = \mathbf{g}_\mathbf{e}(\mathbf{r}_k) u \quad \text{where } \mathbf{g}_\mathbf{e}(\mathbf{r}_i) = \frac{\mu_0 C_0}{4\pi} \int_{V_E} \frac{\mathbf{e}_\theta \times (\mathbf{r}_i - \mathbf{r})}{|\mathbf{r}_i - \mathbf{r}|^3} d\upsilon \tag{14a}$$

$$\frac{\mathbf{B}_{\mathbf{v}kl}}{\mu_r \nu_l} = \mathbf{J}_l \times \mathbf{g}_\mathbf{v}(\mathbf{r}_{kl}) \quad \text{where } \mathbf{g}_\mathbf{v}(\mathbf{r}_{kl}) = \frac{\mu_0}{4\pi s_k \nu_l} \int_{s_k} \int_{\nu_l} \frac{\mathbf{r}_k - \mathbf{r}_l}{|\mathbf{r}_k - \mathbf{r}_l|^3} d\upsilon\, ds \tag{14b}$$

$$\text{and} \quad \frac{\mathbf{B}_{\mathbf{b}ki}}{s_i} = \mathbf{K}_i \times \mathbf{g}_\mathbf{b}(\mathbf{r}_{ki}) \quad \text{where } \mathbf{g}_\mathbf{b}(\mathbf{r}_{ki}) = \frac{\mu_0}{4\pi s_k s_i} \int_{s_k} \int_{s_i} \frac{\mathbf{r}_k - \mathbf{r}_i}{|\mathbf{r}_k - \mathbf{r}_i|^3} ds\, ds. \tag{14c}$$

Similar to (10), the kernel functions ($\mathbf{g_v}$ and $\mathbf{g_b}$) in (14b, c) that describe the EC-generated MFD can be approximated by

$$\mathbf{g}_{(\mathbf{v},\mathbf{b})}(\mathbf{r}_{ij}) \approx \frac{\mu_0}{4\pi} (\mathbf{r}_i - \mathbf{r}_j) \begin{cases} r_{ij}^{-3} & r_{ij} \neq 0 \\ b_j^{-3} & r_{ij} = 0. \end{cases} \tag{15}$$

With the kernel functions in (14a-c), the discrete-form of the surface-current-source in (11) is given by (16) where $\mathbf{I}_{3m}$ is a $3m \times 3m$ identity matrix:

$$\mathbf{K} = \rho (\mathbf{I}_{3m} - \rho \mathbf{G}_2)^{-1} (\mu_r \mathbf{G}_1 \mathbf{J} - \mathbf{h}_2 u); \tag{16}$$

where $\mathbf{h}_2 (\in \mathbb{R}^{3m \times 1}) = [\mathbf{N}][\, \mathbf{g}_\mathbf{e}^\mathrm{T}(\mathbf{r}_1) \cdots \quad \mathbf{g}_\mathbf{e}^\mathrm{T}(\mathbf{r}_k) \cdots \quad \mathbf{g}_\mathbf{e}^\mathrm{T}(\mathbf{r}_m)\,]^\mathrm{T}$;

$$\mathbf{G}_1 \left(\in \mathbb{R}^{3m \times 3n}\right) = [\mathbf{N}] \begin{bmatrix} \nu_1 [\mathbf{g_v}(\mathbf{r}_{11})]_\times \cdots & \nu_l [\mathbf{g_v}(\mathbf{r}_{1l})]_\times \cdots & \nu_n [\mathbf{g_v}(\mathbf{r}_{1n})]_\times \\ \vdots \cdots & \vdots \cdots & \vdots \\ \nu_1 [\mathbf{g_v}(\mathbf{r}_{m1})]_\times \cdots & \nu_l [\mathbf{g_v}(\mathbf{r}_{ml})]_\times \cdots & \nu_n [\mathbf{g_v}(\mathbf{r}_{mn})]_\times \end{bmatrix};$$

$$\mathbf{G}_2 \left(\in \mathbb{R}^{3m \times 3m}\right) = [\mathbf{N}] \begin{bmatrix} s_1 [\mathbf{g_b}(\mathbf{r}_{11})]_\times \cdots & s_i [\mathbf{g_b}(\mathbf{r}_{1i})]_\times \cdots & s_m [\mathbf{g_b}(\mathbf{r}_{1m})]_\times \\ \vdots \cdots & \vdots \cdots & \vdots \\ s_1 [\mathbf{g_b}(\mathbf{r}_{m1})]_\times \cdots & s_i [\mathbf{g_b}(\mathbf{r}_{mi})]_\times \cdots & s_m [\mathbf{g_b}(\mathbf{r}_{mm})]_\times \end{bmatrix};$$

$$\text{and} \quad [\mathbf{N}] = \begin{bmatrix} [\mathbf{n}_1]_\times & \mathbf{0} & \mathbf{0} \\ \mathbf{0} & \ddots & \mathbf{0} \\ \mathbf{0} & \mathbf{0} & [\mathbf{n}_m]_\times \end{bmatrix}.$$

Substituting (16) to (11), $\mathbf{J}$ can be expressed compactly in state-space representation as

$$\dot{\mathbf{J}} = [\boldsymbol{\alpha}]\mathbf{J} + [\boldsymbol{\beta}]\dot{u} + [\boldsymbol{\gamma}]\boldsymbol{\Phi} \tag{17}$$

where $\sigma \mu_r [\boldsymbol{\alpha}] = -(\mathbf{F}_1 + \rho \mathbf{F}_2 \mathbf{L} \mathbf{G}_1)^{-1}$; $[\boldsymbol{\beta}] = \sigma [\boldsymbol{\alpha}] (\mathbf{h}_1 - \rho \mathbf{F}_2 \mathbf{L} \mathbf{h}_2)$; $[\boldsymbol{\gamma}] = \sigma [\boldsymbol{\alpha}] \boldsymbol{\Gamma}$ and $\mathbf{L} = (\mathbf{I}_{3m} - \rho \mathbf{G}_2)^{-1}$. In (17), $\mathbf{J}$ and $\dot{u}$ are the state and input variables respectively, while $\boldsymbol{\Phi}$ is treated as additional unknown.

### 2.1.2. Derivation of constraints on DCS elements

To obtain a unique solution, the continuity and boundary constraints must be appropriately defined to solve for the unknown vectors, $\mathbf{J}$ and $\boldsymbol{\Phi}$. The eddy current density $\mathbf{J}$ must satisfy the continuity equation (3a). For each element in the DCS model, the net current flows out of the six faces (Fig. 2a) must be zero. Mathematically,

$$\sum_{\ell = x,y,z} \left[ s_{i\ell +} (\mathbf{J}_{i\ell +} \bullet \mathbf{n}_{i\ell +}) + s_{i\ell -} (\mathbf{J}_{i\ell -} \bullet \mathbf{n}_{i\ell -}) \right] = 0 \tag{18}$$

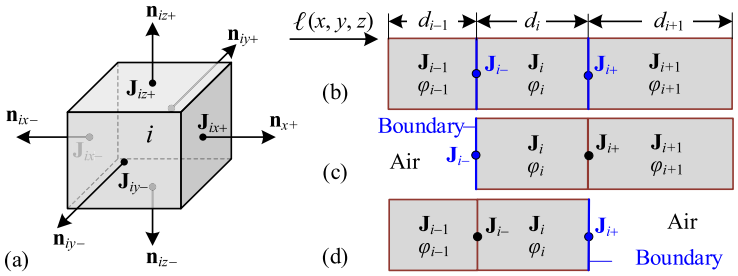


**Fig. 2.** Illustration of constraints imposing method.

where the current density $\mathbf{J}_{i\ell\pm}$ at each elemental surface (area $s_{i\ell\pm}$ and outward normal vector $\mathbf{n}_{i\ell\pm}$) is continuous between its neighboring elements and can be linearly interpolated/extrapolated by equaling the spatial derivatives on both sides of $\mathbf{J}_{i\ell\pm}$. For the $i$th element which is adjacent to $(i-1)$th and/or $(i+1)$th element in the direction $\ell(=x,y,z)$ as illustrated in Figs. 2(b-d), $\mathbf{J}_{i\ell\pm}$ can be obtained based on the surface type (inner/boundary surface) it located in, which can be formulated as:

$$\mathbf{J}_{i\ell\pm} = \begin{cases} \dfrac{d_{i\pm1}}{d_i + d_{i\pm1}}\mathbf{J}_i + \dfrac{d_i}{d_i + d_{i\pm1}}\mathbf{J}_{i\pm1} & \text{inner surface (Fig. 2b)} \\ \dfrac{2d_i + d_{i\mp1}}{d_i + d_{i\mp1}}\mathbf{J}_i - \dfrac{d_i}{d_i + d_{i\mp1}}\mathbf{J}_{i\mp1} & \text{boundary surface (Fig. 2c, d).} \end{cases} \tag{19}$$

Equations (18) and (19) can be assembled as (20):

$$\mathbf{Q}_c\mathbf{J} = \mathbf{0}. \tag{20}$$

The $i$th row of $\mathbf{Q}_c$ represents the continuity equation (18) for the $i$th element. As only $(n-1)$ continuity equations for the $n$ elemental sources are independent, $\mathbf{Q}_c \in \mathbb{R}^{(n-1)\times 3n}$.

In (11), the gradient operation matrix $\boldsymbol{\Gamma}$ of the electric potential is approximated by finite difference methods. The specific method for computing the gradient at the $i$th elemental potential depends on the element type as illustrated in Figs. 2(b, c, d):

Fig. 2(b)
Central difference:
$$\frac{\partial\varphi_i}{\partial\ell} = \begin{bmatrix} \dfrac{-1}{d_i + d_{i-1}} & \dfrac{d_{i-1} - d_{i+1}}{(d_i + d_{i+1})(d_i + d_{i-1})} & \dfrac{1}{d_{i+1} + d_i} \end{bmatrix} \begin{bmatrix} \varphi_{i-1} \\ \varphi_i \\ \varphi_{i+1} \end{bmatrix} \tag{21a}$$

Fig. 2(c)
Forward difference:
$$\frac{\partial\varphi_i}{\partial\ell} = \begin{bmatrix} \dfrac{-2}{d_i + d_{i+1}} & \dfrac{2}{d_i + d_{i+1}} \end{bmatrix} \begin{bmatrix} \varphi_i \\ \varphi_{i+1} \end{bmatrix} \tag{21b}$$

Fig. 2(d)
Backward difference:
$$\frac{\partial\varphi_i}{\partial\ell} = \begin{bmatrix} \dfrac{-2}{d_i + d_{i-1}} & \dfrac{2}{d_i + d_{i-1}} \end{bmatrix} \begin{bmatrix} \varphi_{i-1} \\ \varphi_i \end{bmatrix}. \tag{21c}$$

As shown in (21a, b, c) where $\ell(=x,y,z)$, the gradient of the $i$th elemental potential in $\boldsymbol{\Gamma}$ takes up three rows, $(3i-2)$ to $3i$, where $i = 1, 2, \ldots, n$. Since only the gradient of scalar electric potential, $\nabla\varphi$, in (7) is of interests, the zero $\varphi$ reference that can be arbitrarily specified is written as (22) where the vector $\mathbf{Q}_p(\in \mathbb{R}^{1\times n})$ has one element assigned with 1 and all other elements with 0:

$$\mathbf{Q}_p\boldsymbol{\Phi} = 0. \tag{22}$$

In the following discussion, the potential of the far-field element (the element farthest from EM) is set as zero.

### 2.2. Solutions to discrete ECD and output equation

The discrete state-space equations describing the 3D eddy-current problem are given by the system equation (17), the constraint equation (20) for $\mathbf{J}$ and (22) for $\boldsymbol{\Phi}$. The solutions to the ECD $\mathbf{J}$ depend on the type of the excitation input to the EM coil, which can be derived either in time domain or frequency domain as follows:

Discrete-time domain formulation: The corresponding discrete equivalence (with a zero-order hold) of the distributed eddy-current system (17) for iteratively solving the ECD $\mathbf{J}$ under a time-varying arbitrary input is given by (23) where $\Delta T$ is the sampling period.

$$\mathbf{J}(k+1) = [\bar{\boldsymbol{\alpha}}]\mathbf{J}(k) + [\bar{\boldsymbol{\beta}}]\dot{u}(k) + [\bar{\boldsymbol{\gamma}}]\boldsymbol{\Phi}(k); \quad \mathbf{J}(0) = \mathbf{J}_0 \tag{23}$$

where $[\bar{\boldsymbol{\alpha}}] = \exp^{[\boldsymbol{\alpha}]\Delta T}$; $[\bar{\boldsymbol{\beta}}] = (\int_0^{\Delta T} e^{[\boldsymbol{\alpha}]\lambda} d\lambda)[\boldsymbol{\beta}]$; and $[\bar{\boldsymbol{\gamma}}] = (\int_0^{\Delta T} e^{[\boldsymbol{\alpha}]\lambda} d\lambda)[\boldsymbol{\gamma}]$.

Harmonic formulation: Sinusoidal inputs are commonly used in eddy-current systems. Using the phasor method that replaces $(\dot{\mathbf{J}}, \dot{u})$ as complex variables $(j\omega\mathbf{J}, j\omega u)$ where $j = \sqrt{-1}$ and $\omega$ $(= 2\pi f)$ is angular frequency, the differential equation (17) reduces to an algebraic equation,

$$\big(j\omega\mathbf{I}_{3n} - [\boldsymbol{\alpha}]\big)\mathbf{J} - [\boldsymbol{\gamma}]\boldsymbol{\Phi} = j\omega[\boldsymbol{\beta}]u. \tag{24}$$

Each of the two formulations, discrete-time (23) and frequency domain (24), involves two unknowns; namely, $\mathbf{J}(k+1)$ and $\boldsymbol{\Phi}(k)$ for (23), and the complex $\mathbf{J}$ and $\boldsymbol{\Phi}$ variables for (24). To account for the additional unknown $\boldsymbol{\Phi}$, the constraints (20) and (22) are introduced along with (23) or (24) to construct a compact set of linear equation (25), which can be solved from (26) where $\mathbf{J}$ and $\boldsymbol{\Phi}$ are replaced with $\mathbf{J}(k+1)$ and $\boldsymbol{\Phi}(k)$ when solving the discrete-time solutions:

$$[\mathbf{C}]\begin{bmatrix}\mathbf{J}^{\mathrm{T}} & \boldsymbol{\Phi}^{\mathrm{T}}\end{bmatrix}^{\mathrm{T}} = \begin{bmatrix}\mathbf{b}^{\mathrm{T}} & \mathbf{0}_{1\times n} & 0\end{bmatrix}^{\mathrm{T}} \tag{25}$$

$$\begin{bmatrix}\mathbf{J}^{\mathrm{T}} & \boldsymbol{\Phi}^{\mathrm{T}}\end{bmatrix}^{\mathrm{T}} = [\mathbf{C}]^{-1}\mathbf{b} \tag{26}$$

where $[\mathbf{C}] = \begin{bmatrix}\mathbf{C}_{11} & -[\boldsymbol{\gamma}] \\ \mathbf{Q}_c & \mathbf{0} \\ \mathbf{0} & \mathbf{Q}_p\end{bmatrix}$ is an $4n \times 4n$ matrix; and $\begin{cases}\text{Discrete time: } \mathbf{C}_{11} = \mathbf{I}_{3n}; & \mathbf{b} = [\bar{\boldsymbol{\alpha}}]\mathbf{J}(k) + [\bar{\boldsymbol{\beta}}]\dot{u}(k). \\ \text{Harmonic: } \mathbf{C}_{11} = j\omega\mathbf{I}_{3n} - [\boldsymbol{\alpha}]; & \mathbf{b} = j\omega[\boldsymbol{\beta}]u.\end{cases}$

EC cannot be directly measured but can be evaluated by measuring the EC-generated MFD at the specified location $\mathbf{r}_s$, which is contributed by all the current sources as derived in (14b, c). In matrix form, $\mathbf{B}(\mathbf{r}_s) = [B_{sx} \quad B_{sy} \quad B_{sz}]^{\mathrm{T}} = -\mu_r\mathbf{H}_1\mathbf{J} - \mathbf{H}_2\mathbf{K}$ where $\mathbf{K}$ has been given in (16). Thus, the output equation can be written as

$$\mathbf{B}(\mathbf{r}_s) = \big[-\mu_r\big(\mathbf{H}_1 + \rho\mathbf{H}_2\mathbf{L}^{-1}\mathbf{G}_1\big)\big]\mathbf{J} + \big[\rho\mathbf{H}_2\mathbf{L}^{-1}\mathbf{h}_2\big]u \tag{27}$$

where $\mathbf{H}_1 = [\nu_1[\mathbf{g}_{\mathbf{v}}(\mathbf{r}_{s1})]_\times \cdots \quad \nu_l[\mathbf{g}_{\mathbf{v}}(\mathbf{r}_{si})]_\times \cdots \quad \nu_n[\mathbf{g}_{\mathbf{v}}(\mathbf{r}_{sn})]_\times]$ and $\mathbf{H}_2 = [s_1[\mathbf{g}_{\mathbf{b}}(\mathbf{r}_{s1})]_\times \cdots \quad s_k[\mathbf{g}_{\mathbf{b}}(\mathbf{r}_{sk})]_\times \cdots \quad s_m[\mathbf{g}_{\mathbf{b}}(\mathbf{r}_{sm})]_\times]$.

To summarize, (26) provides the basis to solve EC problem for a conductor with decomposed elements. Once $\mathbf{J}$ is solved, $\mathbf{B}$ can be obtained from (27).

#### 2.2.1. Harmonic solution for an axisymmetric system

For an axisymmetric system where the $\boldsymbol{\Phi}$ term vanishes and the constraint equations are automatically satisfied, the harmonic solutions to $\mathbf{J}$ can be directly obtained from (28):

$$\mathbf{J} = \big[j\omega\big(j\omega\mathbf{I}_{3n} - [\boldsymbol{\alpha}]\big)\big]^{-1}[\boldsymbol{\beta}]u. \tag{28}$$

Since the EC flows only in circumferential direction for an axisymmetric system, the system is modeled with annular elements [25] in cylindrical coordinates. The corresponding kernel functions, $f_{(\mathrm{v,b})}$ and $\mathbf{g}_{(\mathbf{v},\mathbf{b})}$, for the source element located at $\mathbf{r}_j = [r_j \quad 0 \quad z_j]^{\mathrm{T}}$ and target element $\mathbf{r}_i = [r_i \quad 0 \quad z_i]^{\mathrm{T}}$ are given by (29a, b):

$$f_{(\mathrm{v,b})}(r_{ij}) = \frac{\mu_0}{4\pi}\int_0^{2\pi} \frac{r_j\cos\theta d\theta}{\sqrt{(r_i - r_j\cos\theta)^2 + (r_j\sin\theta)^2 + (z_i - z_j)^2}} \tag{29a}$$

$$\mathbf{g}_{(\mathbf{v},\mathbf{b})}(\mathbf{r}_{ij}) = \frac{\mu_0}{4\pi}\int_0^{2\pi} \frac{[(z_i - z_j)\cos\theta \quad 0 \quad r_j - r_i\cos\theta]^{\mathrm{T}} r_j d\theta}{[(r_i - r_j\cos\theta)^2 + (r_j\sin\theta)^2 + (z_i - z_j)^2]^{3/2}}. \tag{29b}$$

### 2.3. Element refinement method

In practical implementation, the sizes of the matrices $(\mathbf{F}_1, \mathbf{F}_2, \mathbf{G}_1, \mathbf{G}_2)$ characterizing the conductor are determined by the number of elements. Denser elements contribute to higher accuracy but at the expense of computing cost and complexity. An element-refinement procedure is developed for effective trade-off between accuracy and efficiency. As will be shown, elements with thin aspect ratios have an adverse effect on the accuracy of the kernel-functions. A method to improve accuracy without increasing the matrix sizes is proposed.

#### 2.3.1. Refinement procedure

The procedure begins with subdividing the thickness into layers to account for the skin-depth effects. The skin-depth $\delta$ of a harmonically excited ECD along the depth $z_h$ can be approximately expressed in (30) where $\mathbf{J}_S$ is the ECD at the surface [24]:

$$\frac{|\mathbf{J}(z_h)|}{|\mathbf{J}_S|} \approx \exp\left(-\frac{z_h}{\delta}\right) \quad \text{where } \delta = \frac{1}{\sqrt{\pi(\mu_0\mu_r\sigma)f}}. \tag{30}$$

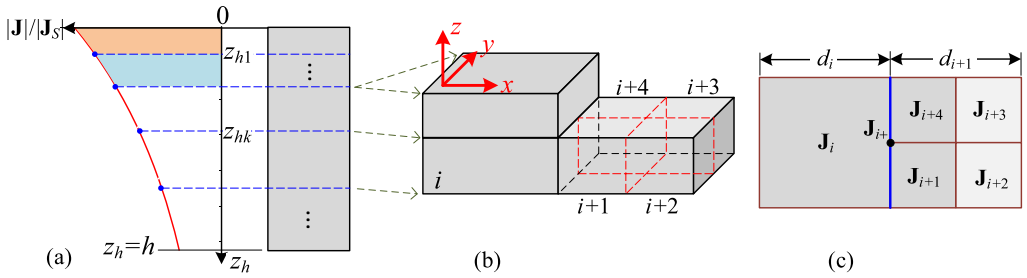


**Fig. 3.** Illustration of refinement. (a) Refinement in $z$-direction. (b) Refinement in $x$-$y$ plane. (c) Plane view of refined element.

For improving the resolution in modeling the skin-depth, the layers along the depth are subdivided such that the integrated ECs (shaded areas under the $\mathbf{J}/\mathbf{J}_s$ curve as illustrated in Fig. 3a) in each layer are approximately the same. Mathematically, the depths at each interface for a conductor (with thickness $h$) are divided into $n_h$ layers as given by (31):

$$\frac{z_{hi}}{\delta} = -\ln\left[1 - \frac{i}{n_h}\left(1 - e^{-h/\delta}\right)\right] \quad \text{where } i = 1, 2, \ldots, n_h - 1. \tag{31}$$

In this paper, $n_h$ that represents the refinement level is decided by ensuring the decrease of EC density in each layer less than 20%.

Next, the elements (with high ECD gradients) in each layer are subdivided (Fig. 3b). To detect the boundary effects and regions where changes in the ECD distribution are dominant in each layer, the ECD gradient tensor is defined by (32) for the $i$th element:

$$\mathbf{T}_i = \begin{bmatrix} \partial J_{ix}/\partial x & \partial J_{ix}/\partial y \\ \partial J_{iy}/\partial x & \partial J_{iy}/\partial y \end{bmatrix}. \tag{32}$$

To facilitate implementing the matrixes ($\mathbf{Q}_c$ and $\boldsymbol{\Gamma}$), the refinements are performed by partitioning the elements into four sub-elements. The criterion for whether or not sub-dividing an element can be determined by the Frobenius norm of $\mathbf{T}_i$, which is

$$T_i = \sqrt{\mathrm{tr}\left(\mathbf{T}_i^{\mathbf{T}}\mathbf{T}_i\right)}. \tag{33}$$

If $T_i > \kappa T_{\max}$ where $\kappa$ is the scale factor of threshold and $T_{\max}$ is the maximum value in $\mathbf{T}_i$, the element is divided.

With the refined elements, the matrices ($\mathbf{Q}_c$ and $\boldsymbol{\Gamma}$) are computed similarly as in (19) and (21) except at the boundary surface as illustrated in Fig. 3(c) where the current density $\mathbf{J}_{i+}$ is approximated by interpolating from all of its adjacent elements; $\mathbf{J}_i$ of the original element, and $\mathbf{J}_{i+1}$ and $\mathbf{J}_{i+4}$ of the sub-elements:

$$\mathbf{J}_{i+} = \frac{d_{i+1}}{2d_i + d_{i+1}}\mathbf{J}_i + \frac{d_i}{2d_i + d_{i+1}}(\mathbf{J}_{i+1} + \mathbf{J}_{i+4}). \tag{34}$$

The $\varphi$ gradient of these elements can be obtained through single-sided difference as shown in (21b, c).

*2.3.2. Effect of approximate kernel functions on accuracy*

The approximate kernel functions, (10) and (15), treat the volume/surface elements as unit point sources to calculate the MVP and MFD between two elements. The element aspect-ratio has an effect on the approximation accuracy as numerically illustrated in Fig. 4, where the MVP and MFD simulated by (10) and (15) are compared with the integral solutions in (9b, c) and (14b, c) for two different element types; cube (1:1:1) in Fig. 4(a) and half-cube (2:2:1) in Fig. 4(b). As compared in Fig. 4, the approximate kernel functions demonstrate good approximations when the observed point is far from the source elements. The approximated MVP and MFD between two cubic elements show excellent agreements with the integral solutions in Fig. 4(a) but for the half-cubic elements (Fig. 4b), the approximation errors increase as the observed point is closer to the source element; implying that the kernel function approximations approach the integral solutions as the element shape approaches a (1:1:1) aspect-ratio.

To maintain accuracy without increasing the matrix sizes, each thin-element is "virtually" divided into approximately cubic sub-elements as illustrated in Fig. 4(c). In Fig. 4(c), $d_{i\ell}$ and $d_{j\ell}$ ($\ell = x, y, z$) are the side lengths for the $i$th volume and $j$th surface elements; $b_i$ and $b_j$ are the bounding radii; and $r$ is the distance to the other (target or source) element. Based on the distance/bounding-radius ratio, the element can be evenly divided into $N_i$ and $N_j$ approximately cubic/square elements as defined in (35a, b) where $d_0 = \min(d_{i\ell}, d_{j\ell}, r)$, [*] denotes rounding operation and the multiplication factor $k$ increases the number of virtual divisions:

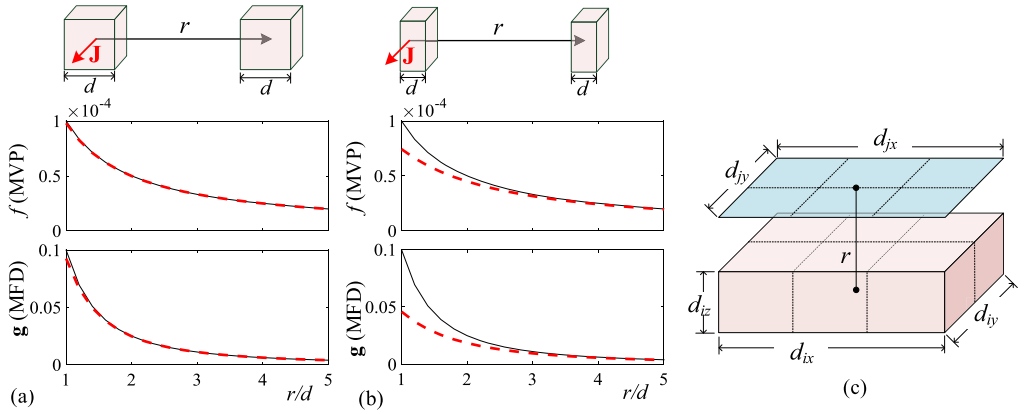


**Fig. 4.** Comparison of kernel function and integral method. (a) Cube elements. (b) Half-cube elements. (c) Illustration of virtual subdivision.

**Table 1**
EM and conductor parameters for 2D axisymmetric system.

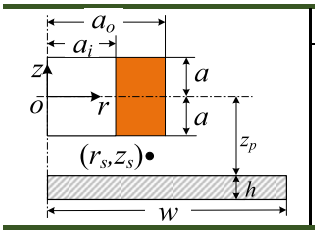


| EM | | Plate | Case 1a) | Case 1b) |
|---|---|---|---|---|
| ($a_o$, $a_i$, $a$) mm | (6, 3.75, 2) | $w$ (mm) | 12, 24 | 36 |
| # of turns | 60 | $h$ (mm) | 2 | 1 |
| $f$ (Hz) | 1000 | $z_p$ (mm) | 5.5 | 5.5 |
| Amplitude (A) | 1 | $\sigma$ (MS/m) | 10 | 1.45 |
| | | $\mu_r$ | 1, 10 | $\approx 1$ |

$$N_i = \begin{cases} 1 & r > 3 \cdot \max(b_i, b_j) \\ k \prod_{\ell} [d_{i\ell}/d_0] & r \le 3 \cdot \max(b_i, b_j) \end{cases} \tag{35a}$$

$$\text{and} \quad N_j = \begin{cases} 1 & r > 3 \cdot \max(b_i, b_j) \\ k \prod_{\ell} [d_{j\ell}/d_0] & r \le 3 \cdot \max(b_i, b_j). \end{cases} \tag{35b}$$

The improved kernel functions then can be expressed as the average effects of the sub-elements:

$$\hat{f}_{(\mathrm{v,b})}(r_{ij}) = \frac{1}{N_j \cdot N_i} \sum_{q=1}^{N_j} \sum_{p=1}^{N_i} f_{(\mathrm{v,b})}(r_{pq}); \tag{36a}$$

$$\text{and} \quad \hat{\mathbf{g}}_{(\mathbf{v},\mathbf{b})}(\mathbf{r}_{ij}) = \frac{1}{N_j \cdot N_i} \sum_{q=1}^{N_j} \sum_{p=1}^{N_i} \mathbf{g}_{(\mathbf{v},\mathbf{b})}(\mathbf{r}_{pq}). \tag{36b}$$

## 3. Verification of the DCS method

The DCS modeling method, which accounts for the magnetization and boundary effects, has been validated numerically and experimentally with results organized into three cases:

Case 1 (2D axisymmetric harmonic model): The DCS harmonic solutions derived in (28) with kernel functions for axisymmetric annular elements (29a, b) are verified analytically in Case 1a) and experimentally in Case 1b), where the EM/plate configuration and parametric values for the 2D simulation in cylindrical coordinates are given in Table 1.

1a) The boundary and magnetization effects on the eddy-current were numerically analyzed and validated with analytical solutions [6] for four different conductors; two radii (24 mm and 12 mm) and two permeability values ($\mu_r = 1$ and 10). To help visualize, Fig. 5 plots the (real, imaginary) parts of the ECD at the depth of 0.25 mm.
1b) The magnetization effects on the induced eddy current was experimentally investigated on an existing testbed [1] with an austenitic 304L stainless-steel plate, which is nonmagnetic but can be weakly magnetized after cold work. The EC-generated MFDs were measured (at $r_s = 6$ mm, $z_s = -3.5$ mm) and compared with two simulations; nonmagnetic

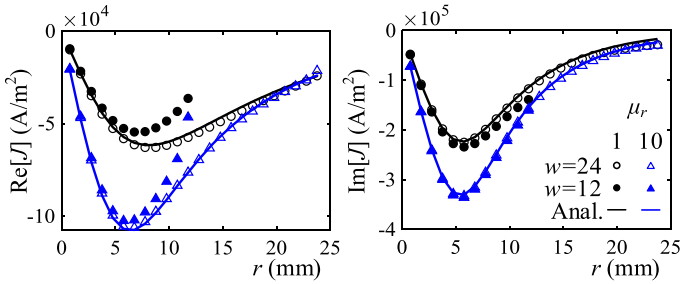


**Fig. 5.** ECD response of axisymmetric system (verified with analytical solution).

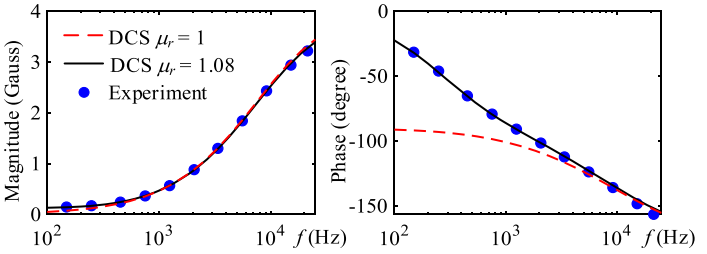


**Fig. 6.** MFD response of stainless-steel plate (experimental validation).

**Table 2**
Configuration and parameters of TEAM problem 7 [26].

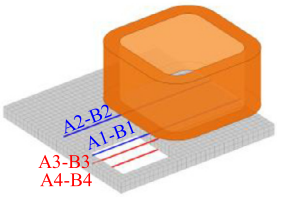


| **Square-ring EM** | **% Error relative to [26]** | | |
|---|---|---|---|
| Ampere-turns: 2742 (AT) | **MFD** | **J-$\varphi$ model** | CLS [20] |
| Frequency: 50, 200 (Hz) | A1-B1 | 0.95% | 5.30% |
| **Conductor** | A2-B2 | 2.30% | 13.6% |
| Dimension: 294×294×19 (mm) | **ECD** | | |
| Conductivity: 35.26MS/m | A3-B3 | 1.76% | 3.83% |
| Number of elements: 1760 | A4-B4 | 7.35% | 11.11% |

plate ($\mu_r = 1$), and plate with a very weak permeability ($\mu_r = 1.08$). The frequency response (magnitude and phase plots) of the measured MFD for the operating frequency ranging from 100 Hz to 25 kHz are shown in Fig. 6.

Case 2 (3D harmonic model): Unlike Case 1 where the continuity equation (20) is automatically satisfied, the 3D models account for the geometrical and magnetization effects on the DCS modeled eddy current. Two models, Case 2a) and Case 2b) for a nonmagnetic and a magnetic conductor respectively, were numerically illustrated:

2a) A DCS model was formulated for the EM/plate configuration of the TEAM Problem 7 shown in Table 2, where published data [26] obtained experimentally at two exciting frequencies, $f = 50$ and 200 Hz for a *nonmagnetic* conductor are available for validation. The MFD and ECD responses are computed and compared with that reported in [20] where the eddy current system is formulated as a constrained least-square (CLS) problem to solve **J** from (17) but without the third term (that models the effect of electric potential $\varphi$). The results, which show $B_z$ along the A1-B1 and A2-B2 lines in the air space above the conductor and $J_y$ along the A3-B3 and A4-B4 lines on the top and bottom surfaces of the conductor as indicated in Table 2, are summarized in Figs. 7(a, b). The average computing errors relative to experimental data [26] are tabulated in Table 2 (third column).

2b) The element-refinement method to improve modeling accuracy of the DCS model based on the **J**-$\varphi$ formulation is numerically illustrated using the non-symmetric EM/plate configuration with a magnetic conductor shown in Table 3 where the parametric values used are listed. For 3D problems where analytical solutions and experimental data accounting for the magnetization and boundary effects on the induced eddy current are not available, the commercial FEA software (COMSOL Multiphysics) was utilized as a basis for comparison. The FEA model is shown in Table 3, where the EM and plate are enclosed by a spherical air domain ($R = 50$ mm) utilizing its *Infinite Element Domain* feature, which is not required by the DCS model. The results are summarized in Fig. 8 and Fig. 9.

Case 3 (3D discrete-time model): The time-domain DCS formulation (26), which provides a straightforward approach to solve EC problems under an arbitrary current excitation, is numerically validated by comparing results with that simulated

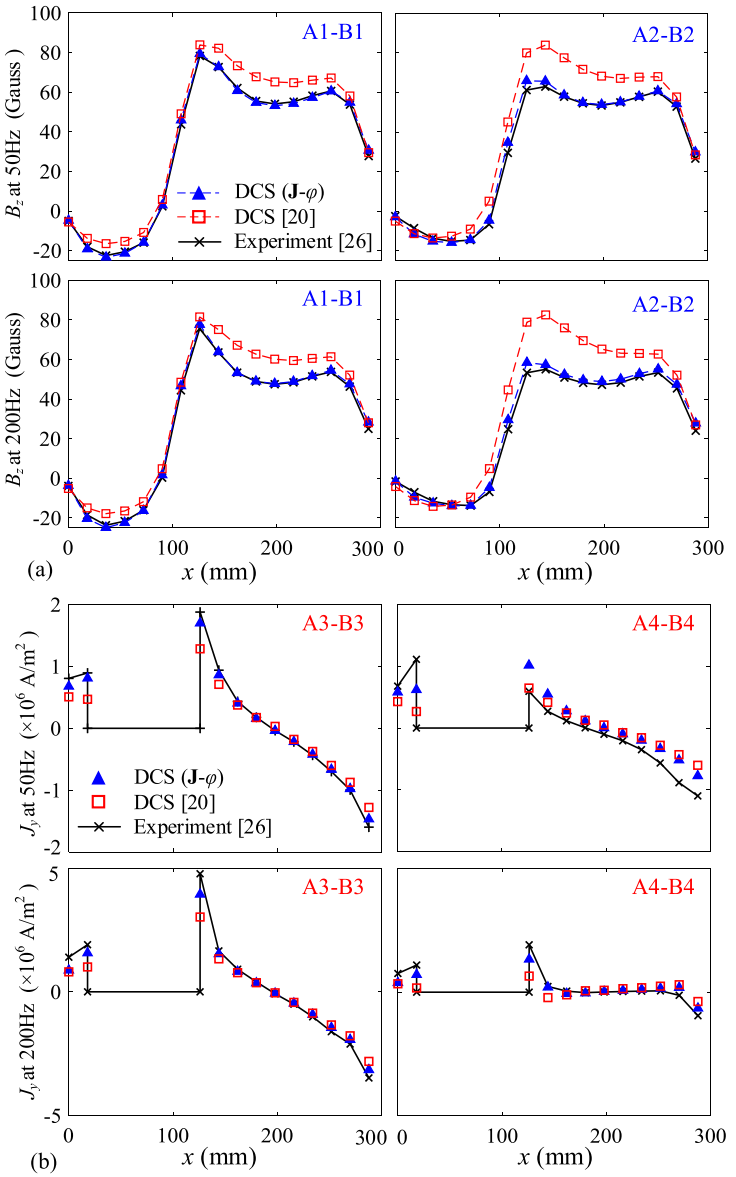


**Fig. 7.** Results for TEAM problem 7. (a) $B_z$ at line A1-B1 and A2-B2. (b) $J_y$ at line A3-B3 and A4-B4.

**Table 3**
Configuration and parameters of magnetic conductor.

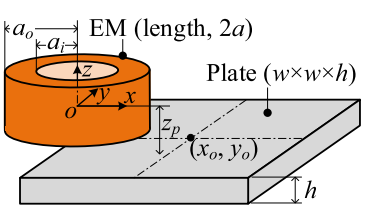


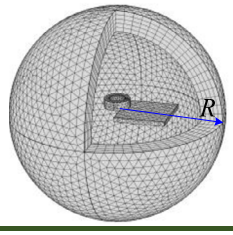


| | |
|---|---|
| **EM** (same with Table 1) | |
| **Conductor** | |
| ($w$, $h$; $z_p$) | (24, 2; 5.5) mm |
| ($x_o$, $y_o$) | (12, 6) mm |
| $\sigma$, $\mu_r$ | 5.27 MS/m, 10 |
| **MFD sensor** location | $x$ = −12:1:12 mm<br>$y = z = 0$ |
| **FEA** | $R$ = 50 mm |

in COMSOL. In this study, a rectangular pulse signal with time-constant $\tau = 10$ μs (that accounts for the 1st order EM dynamics) was employed as an input excitation to investigate the effects of the hidden rectangular blind-hole (simulating a defect) on the $B_z$ measured between the EM center and the plate as shown in Table 4 where the parametric values are summarized. The time-domain solutions were iteratively solved with a sampling period $\Delta T$ of 1 μs. The EC-generated $B_z$

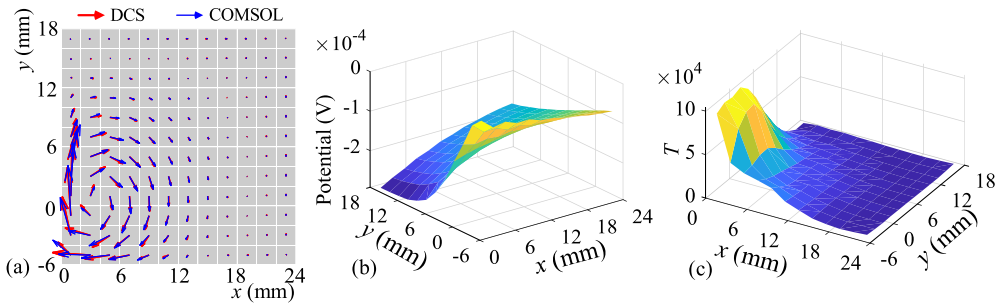


**Fig. 8.** Initial results for magnetic conductor. (a) ECD (verified with COMSOL). (b) Electric potential. (c) Tensor norm for ECD distribution.

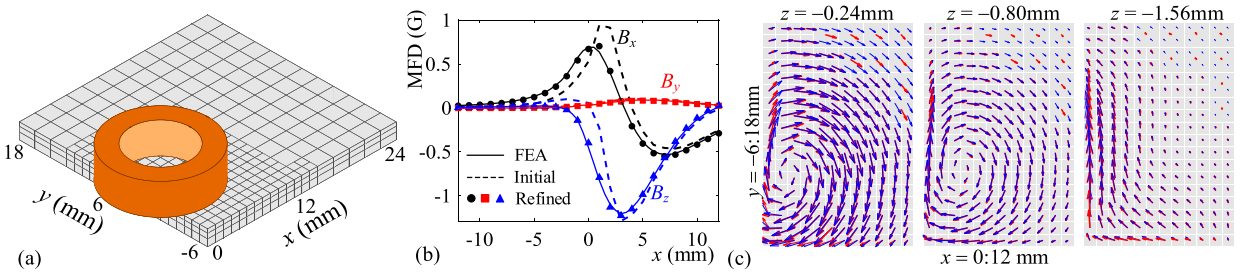


**Fig. 9.** Results after element refinement. (a) Illustration of refined elements. (b) MFD distribution before/after refinement. (c) ECD distribution in refined elements.

**Table 4**
Excitation signal and EM/plate configuration.

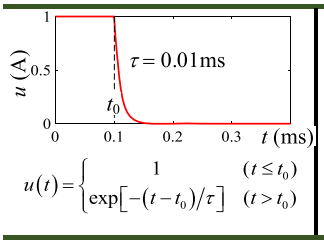


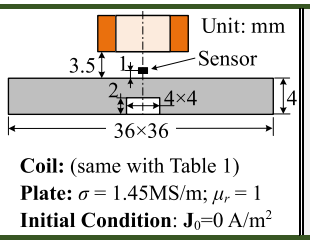


| Method | DCS | FEA |
|---|---|---|
| Element size (mm) | 2×2×1 | 0.32~4.4 |
| Number of elements | 1,288 | 48,588 |
| Degrees of freedom | 5152 | 345,992 |
| Computing time (min) | 1.4 | 31 |

of the plate with the tiny defect is simulated in Fig. 10(a); and the differential signal ($\Delta B_z = B_z - B_{zN}$ where $B_{zN}$ is the EC-generated MFD of the conductor without the defect) commonly used in defect-detection applications is simulated in Fig. 10(b).

All computations are performed on a PC with Intel Core i7-4770, 3.4 GHz CPU, 32 GB RAM and 64-bit OS. The findings from Figs. 5 to 10, where the ECD is solved from (28) for 2D case and (26) for 3D case, are summarized and discussed as follows:

- Fig. 5 plots the (real, imaginary) parts of the ECD distribution. As compared in Fig. 5, the ECD induced in the *magnetic* material ($\mu_r = 10$, denoted by △ and ▲) are much larger than that in *nonmagnetic* conductor ($\mu_r = 1$, denoted by ○ and ●). Fig. 5 further illustrates the *boundary* effects on the ECD models in terms of the conductor-to-EM aspect ratio (defined here as the plate-radius divided by the outer-radius of the EM). When the aspect ratio is 4 (24 mm-radius plate), both the DCS-model and analytical solutions (that assume a conductor with an infinitely large radius) are nearly identical. However, for 12 mm-radius plate that has an aspect ratio of 2, the analytical curves (especially their real part) deviate from the DCS-model (that accounts for the boundary effects) near the boundary region.
- Fig. 6 plots the (magnitude, phase) of the DCS models with/without accounting for the very small permeability ($\mu_r = 1.08$), which are compared with the measured EC-generated MFD for a range of operating frequency. While both models ($\mu_r = 1$ and 1.08) have a nearly identical magnitude curve very close to that obtained experimentally, their phase curves differ significantly under low-frequency ($f < 1$ kHz) operations. When the very small permeability is accounted for in the DCS model, both the magnitude and phase curves agree well with the experimental measurements, implying that the proposed method is capable of revealing the effects of very small relative permeability on the phase response of the EC-generated MFD, which has been commonly ignored in methods assuming non-magnetic materials.

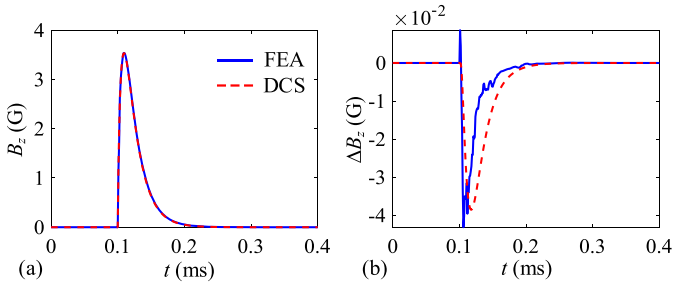


**Fig. 10.** Transient response under pulsed current excitation. (a) MFD response of defective conductor. (b) Differential signal $\Delta B_z$.

- Figs. 7(a, b) compare the proposed model with that reported in [20] where **J** was solved from the constrained least-square problem without the third term in (17). In Fig. 7(b), the values are extrapolated from the ECD computed at the element centers; to improve accuracy, the conductor was decomposed into four layers. As demonstrated in Fig. 7(a, b) and Table 2, the results show that the proposed DCS model based on the **J**-$\varphi$ formulation agrees well with published data [26] with less than 3% and 8% errors in the computed MFD and ECD respectively, which represent a significant improvement over the CLS method [20]. The discrepancy in the ECD solutions could be due to errors caused by the extrapolation.
- Fig. 8(a) compares the DCS-modeled ECD field (imaginary part) with the COMSOL FEA simulation for a magnetic square plate, where the EM is placed near the left edge of the 2 mm-thick conductor divided into cubic-volume and square-surface elements with 2 mm-lengths. Relatively large electric potential gradients near the left edge of the conductor can also be seen in Fig. 8(b). Based on simulated results shown in Figs. 8(a, b), the tensor **T** and its norm $T$ defined in (32) and (33) are calculated in Fig. 8(c), where the elements close to the EM have a much larger norm value; thus, they are subdivided in the $x$ and $y$ directions based on threshold factor $\kappa = 0.1$ to improve computational accuracy. The refined elements are shown in Fig. 9(a) where the thickness ($z$ direction) is sub-divided into three layers based on the criterion illustrated in (31). Fig. 9(b) graphs the EC-generated MFD components along the $x$-direction at ($y = 0$, $z = -4.5$) computed using two DCS-models; namely, the initial single-layer uniform elements in Fig. 8(a), and the refined three-layer elements in Fig. 9(a). As compared in Fig. 9(b), the single-layer DCS model with uniform elements yields reasonably good solutions consistent with that simulated using COMSOL within 4.2% difference defined in (37). The computing accuracy can be significantly improved by accounting for the edge effects with more refined elements; and the three-layer DCS model with refined elements matches the COMSOL FEA within 1.3% difference.

$$\%Difference = \sum_{\ell=x,y,z} |B_{\ell D} - B_{\ell F}|/(3 \times range). \tag{37}$$

- Fig. 9(c) compares the ECD distributions at three different depths ($-0.24$, $-0.8$ and $-1.56$ mm from the plate surface), which reveals no eddy current loops in the 3rd layer ($z = -1.56$ mm). This phenomenon suggests that the EC has a z-component even though the excitation current exists only in the $x$-$y$ plane, which also indicates that multi-layer refinement is necessary for systems with significant edge and skin effects to yield accurate solutions.
- Fig. 10(a) compares the EC-generated $B_z$ modeled by the DCS method with COMSOL FEA simulation for the plate with a tiny hidden defect (Table 4), which shows good agreement. However, some discrepancies can be seen in Fig. 10(b) where the $\Delta B_z = B_z - B_{zN}$ differential curves between the FEA and DCS modeled results are compared. Fig. 10(b) reveals some unsmooth fluctuations that may be caused by computing error in the FEA simulations. As compared in Table 4 (last column), the DCS method which requires much smaller number of elements and degrees-of-freedom than the FEA takes 84 seconds (or less than 5% of that taken by FEA) to solve the problem.

## 4. Illustrative application

The effectiveness of the DCS modeling method is best illustrated in the context of a manufacturing application [5]. The ECD solutions (26) and the MFD model (27) along with the designed (geometrical/conductivity) values are used to establish a reference $\mathbf{B}_{ref}$ (perfect conductor) to detect/locate the hidden (non-conductive cavity) defects from the measurements $\mathbf{B}_{meas}$ using an array of $p$ ($l$-axis) sensors. The reference is formulated as a nonsingular detection matrix [**D**] defined mathematically in (38a) where the $i$th column $\mathbf{d}_i$ characterizes the MFD change caused by the conductor with and only with $i$th cavity element:

$$[\mathbf{D}]\left(\in \mathbb{R}^{pl\times n}\right) = [\mathbf{d}_1 \cdots \quad \mathbf{d}_i \cdots \quad \mathbf{d}_n] \tag{38a}$$

$$\text{where} \quad \mathbf{d}_i = \left[\mathbf{B}_{1i}^{\mathrm{T}} \cdots \quad \mathbf{B}_{ki}^{\mathrm{T}} \cdots \quad \mathbf{B}_{pi}^{\mathrm{T}}\right]^{\mathrm{T}} - \mathbf{B}_{ref}. \tag{38b}$$

**Table 5**
Parameters and result for computing [**D**] matrix.

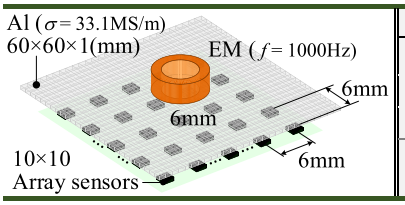


| Method | DCS | FEA |
|---|---|---|
| **Element size (mm)** | 2×2×1 | 1.2~9.2 |
| **Element number** | 900 | 75,831 |
| **Degrees of freedom** | 3600 | 519982 |
| **Average time for computing each column of [D]:** | 2.3s | 64s |

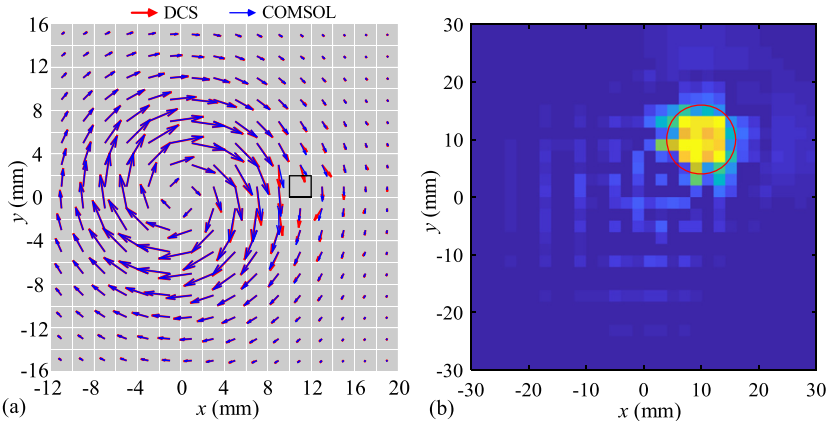


**Fig. 11.** Simulation results. (a) ECD distribution in conductor with single cavity element. (b) Reconstruction result. (For interpretation of the colors in the figure(s), the reader is referred to the web version of this article.)

In (38b), the $k$th measurement $\mathbf{B}_{ik}$ (or the EC-generated MFD of the conductor assuming that the $i$th element is a cavity) can be pre-calculated from (27) where the ECD is solved in (26). Thus, [**D**] requires solving the closed-form solutions $n$ times.

To improve the computing efficiency, a position matrix [**P**] (that assigns the $i$th element with zero ECD) is introduced so that the solutions for a perfect conductor can be modified to establish (the $i$th column $\mathbf{d}_i$ in) [**D**]. As an illustration, consider ([**C**], **b**) in (26) for the case of harmonic excitations,

$$[\mathbf{C}] = \begin{bmatrix} j\omega\mathbf{I}_{3n} - [\mathbf{P}][\boldsymbol{\alpha}] & -[\mathbf{P}][\boldsymbol{\gamma}] \\ \mathbf{Q}_c & \mathbf{0} \\ \mathbf{0} & \mathbf{Q}_p \end{bmatrix}; \quad \mathbf{b} = j\omega[\mathbf{P}][\boldsymbol{\beta}]u \tag{39}$$

where $[\mathbf{P}](\in \mathbb{R}^{3n\times 3n}) = diag(\mathbf{p} \otimes [1\ 1\ 1]^{\mathrm{T}})$ with $\otimes$ stands for Kronecker product; the $n \times 1$ vector **p** with elements equal 1 (regular conductor) or 0 (cavity). In other words, all elements of **p** (except its $i$th element is 0) are set to 1 when calculating the ECD in conductor with $i$th element as cavity. In (39), the matrices ($[\boldsymbol{\alpha}]$, $[\boldsymbol{\beta}]$, $[\boldsymbol{\gamma}]$ and $\mathbf{Q}_c$, $\mathbf{Q}_p$) are calculated for a perfect conductor without any cavity. With (39), each of the $i$th column in [**D**] can be calculated from (26) and (27). Once detection matrix [**D**] and the reference $\mathbf{B}_{ref}$ (perfect conductor) are established, the geometrical field can be reconstructed using the regularization method proposed in [5] to evaluate the probability vector $\tilde{\mathbf{p}}(\in \mathbb{R}^{n\times 1})$ that has a value between 0 (conductive) and 1 (non-conductive) indicating the likelihood that the element is electrically non-conductive.

$$\tilde{\mathbf{p}} = \left([\mathbf{D}]^{\mathrm{T}}[\mathbf{D}] + \lambda[\mathbf{I}]\right)^{-1}[\mathbf{D}]^{\mathrm{T}}(\mathbf{B}_{meas} - \mathbf{B}_{ref}). \tag{40}$$

In (40), $\lambda$ is the regularization parameter which can be determined using the L-Curve method [27]. In this paper, the MATLAB computing package [28] is utilized to calculate (40).

The DCS modeling method for the application is numerically evaluated and compared with results of COMSOL FEA using the setup and parametric values given in the 1st column of Table 5, where the test conductor is placed between the EM and an array of 10 × 10 of 3-axis sensors which contribute to a total of $pl = 300$ measurement data. With an estimated $\delta = 2.8$ mm (larger than the plate thickness of 1 mm), the conductor is decomposed into a single layer of 900 regular hexahedron DCS elements. The FEA was modeled with over 75 K elements including the air space. Simulated results are shown in Fig. 11.

Fig. 11(a) compares the ECD distribution in a plate that has one cavity element computed using the DCS modeling method with that simulated in COMSOL, which provides the basis to compute [**D**]. The average computing time for each column of [**D**] ($\in \mathbb{R}^{300\times 900}$) are compared in the last row of Table 5, showing that the DCS method took only 2.3 s to solve (or less than 4% of that required by the FEA software). Furthermore, the proposed DCS model uses closed-form solutions

that do not require re-meshing of elements generally needed in conventional FEA methods when calculating each column in [**D**]. To help visualize, Fig. 11(b) shows the reconstructed geometrical field for a plate with a hole (denoted by red circle) located at (10 mm, 10 mm) using (40) and matrix [**D**] computed from proposed method. The result shows the location of the hole can be successfully estimated from the reconstruction.

## 5. Conclusion

The DCS-based modeling method for 3D EC problems in magnetic conductor has been presented. The EC and magnetization effects are formulated as ECD sources and surface/volume current-density sources, respectively. Electric potential is introduced into the formulation to account for the boundary effects. The governing equations of the EC problems are formulated in state-space representation with ECD **J** in conductor as primary state-variable and electric potential $\varphi$ as additional unknown, which are solved along with the continuity equation of the EC. The state-space representation makes it convenient to perform time domain analysis where the transient response can be easily obtained by discretizing the continuous system and solve the response iteratively. As a special and most widely used case, the closed-form solution for harmonic excitation is also derived, which can be obtained by solving simple linear equations. The accuracy and effectiveness of the model have been validated by comparing results with analytical solutions, FEA as well as experimental data. It has been shown that the method can accurately solve 2D axisymmetric and 3D EC problems in both nonmagnetic and magnetic conductor. The element refinement method that accounts for the skin-effect and the EC in boundary regions is also illustrated with numerical examples. The ability to model magnetic conductors and account for geometric boundaries demonstrates the potentials of the model in analyzing nondestructive testing and measurement applications. The efficiency and advantage of the modeling method has been illustrated with a field-reconstruction application where a parametric study is often needed to model conductors with small variances. The method is computationally more efficient than FEA because there is no need to repetitively modeling the conductor. It also suggests that the proposed method is ideal for applications where the conductor matrices ($\mathbf{F}_1$, $\mathbf{F}_2$, $\mathbf{G}_1$, $\mathbf{G}_2$) can be pre-calculated. The work required in these problems is only to modify the linear equation slightly and solving it.

## Declaration of competing interest

The authors declare that they have no known competing financial interests or personal relationships that could have appeared to influence the work reported in this paper.

## Acknowledgements

This work was supported in part by the U.S. National Science Foundation under Grant CMMI-1662700, and in part by the National Basic Research Program of China (973 Program) under Grant 2013CB035803.

## Appendix A

Consider Fig. 1(b) showing an external MFD $\mathbf{B}$ ($=\mathbf{B_n}+\mathbf{B_t}$) on the conductor boundary, where $\mathbf{B_n}$ and $\mathbf{B_t}$ are the normal and resultant tangential components of $\mathbf{B}$ respectively; and the MFDs ($\mathbf{B}_+, \mathbf{B}_-$) on the (conductor, air) sides of the boundary satisfy (A.1a, b) [24] where only the normal component of MFD across the boundary is continuous:

$$\mathbf{B}_+ \bullet \mathbf{n} = \mathbf{B}_- \bullet \mathbf{n}; \tag{A.1a}$$

$$\text{and} \quad (\mathbf{B}_+/\mu_r - \mathbf{B}_-) \times \mathbf{n} = 0 \tag{A.1b}$$

$$\text{where} \quad \mathbf{B}_\pm = \mathbf{B_n} + \mathbf{B_t} \pm \tilde{\mathbf{B}}_\mathbf{t}. \tag{A.1c}$$

In (A.1c), $\tilde{\mathbf{B}}_\mathbf{t}$ accounts for the discontinuity in the tangential components (A.1b) due to the magnetizing surface current density $\mathbf{K}$. Substituting (A.1c) into (A.1b) yields

$$\mathbf{B_t} + \tilde{\mathbf{B}}_\mathbf{t} = \mu_r(\mathbf{B_t} - \tilde{\mathbf{B}}_\mathbf{t}); \tag{A.2a}$$

$$\text{and} \quad \mathbf{B}_+ = \mathbf{B_n} + \frac{2\mu_r}{\mu_r+1}\mathbf{B_t}. \tag{A.2b}$$

From (2b), the magnetization vector at the boundary (denoted with $\mathbf{M}_+$) can then be written in terms of $\mathbf{B}_+$ as

$$\mathbf{M}_+ = \frac{\mu_r - 1}{\mu_0 \mu_r}\mathbf{B}_+. \tag{A.3}$$

Hence, the magnetizing surface current density $\mathbf{K}$ can be expressed as

$$\mathbf{K} = \mathbf{M}_+ \times \mathbf{n} = \frac{2}{\mu_0}\frac{\mu_r - 1}{\mu_r + 1}\mathbf{B_t} \times \mathbf{n} = \rho \mathbf{B} \times \mathbf{n} \quad \text{where } \rho = \frac{2}{\mu_0}\frac{\mu_r - 1}{\mu_r + 1}. \tag{A.4}$$

## References


[1] K.-M. Lee, B. Hao, M. Li, K. Bai, Multi-parameter eddy-current sensor design for conductivity estimation and simultaneous distance and thickness measurements, IEEE Trans. Ind. Inform. 15 (3) (2019) 1647–1657.
[2] A. Bermúdez, C. Reales, R. Rodríguez, P. Salgado, Numerical analysis of a finite-element method for the axisymmetric eddy current model of an induction furnace, IMA J. Numer. Anal. 30 (3) (2010) 654–676.
[3] R. Merwa, K. Hollaus, B. Brandstätter, H. Scharfetter, Numerical solution of the general 3D eddy current problem for magnetic induction tomography (spectroscopy), Physiol. Meas. 24 (2) (2003) 545.
[4] N. De Geeter, G. Crevecoeur, L. Dupré, Eddy-current simulations using an independent impedance method in anisotropic biological tissues, IEEE Trans. Magn. 47 (10) (2011) 3845–3848.
[5] M. Li, K.-M. Lee, Machine perception based on field reconstruction for conductivity and hidden geometrical feature characterization, in: 2018 IEEE/ASME International Conference on Advanced Intelligent Mechatronics (AIM), 2018, pp. 510–515.
[6] C. Dodd, W. Deeds, Analytical solutions to eddy-current probe-coil problems, J. Appl. Phys. 39 (6) (1968) 2829–2838.
[7] T. Theodoulidis, E. Kriezis, Series expansions in eddy current nondestructive evaluation models, J. Mater. Process. Technol. 161 (1–2) (2005) 343–347.
[8] R. Albanese, G. Rubinacci, Finite element methods for the solution of 3D eddy current problems, Adv. Imaging Electron Phys. 102 (1997) 1–86.
[9] O. Bíró, Edge element formulations of eddy current problems, Comput. Methods Appl. Mech. Eng. 169 (3-4) (1999) 391–405.
[10] H. Hoshikawa, K. Koyama, M. Maeda, Role of electric potential in eddy current testing phenomena, AIP Conf. Proc. 615 (1) (2002) 380–387.
[11] T. Nakano, Y. Kawase, T. Yamaguchi, M. Nakamura, Parallel computing of 3-D eddy-current analysis with A-$\phi$ method for rotating machines, IEEE Trans. Magn. 48 (2) (2012) 975–978.
[12] Z. Ren, T-$\Omega$ formulation for eddy-current problems in multiply connected regions, IEEE Trans. Magn. 38 (2) (2002) 557–560.
[13] P. Bettini, R. Benato, S.D. Sessa, R. Specogna, T-$\Omega$ formulation for eddy-current problems with periodic boundary conditions, IEEE Trans. Magn. 53 (6) (2017) 1–4.
[14] A.A. Rodriguez, E. Bertolazzi, R. Ghiloni, A. Valli, Finite element simulation of eddy current problems using magnetic scalar potentials, J. Comput. Phys. 294 (2015) 503–523.
[15] H. Feng, X. Cui, G. Li, A stable nodal integration method for static and quasi-static electromagnetic field computation, J. Comput. Phys. 336 (2017) 580–594.
[16] S. Xie, Z. Chen, T. Takagi, T. Uchimoto, Efficient numerical solver for simulation of pulsed eddy-current testing signals, IEEE Trans. Magn. 47 (11) (2011) 4582–4591.
[17] P. Beckstein, V. Galindo, V. Vukčević, Efficient solution of 3D electromagnetic eddy-current problems within the finite volume framework of OpenFOAM, J. Comput. Phys. 344 (2017) 623–646.
[18] A. Trakic, H. Wang, F. Liu, H.S. Lopez, S. Crozier, Analysis of transient eddy currents in MRI using a cylindrical FDTD method, IEEE Trans. Appl. Supercond. 16 (3) (2016) 1924–1936.
[19] J. Lim, K.-M. Lee, Distributed multilevel current models for design analysis of electromagnetic actuators, IEEE/ASME Trans. Mechatron. 20 (5) (2015) 2413–2424.
[20] C.-Y. Lin, K.-M. Lee, B. Hao, Distributed current source method for modeling magnetic and eddy-current fields induced in nonferrous metallic objects, IEEE/ASME Trans. Mechatron. 23 (3) (2018) 1038–1049.
[21] A. Drake, C. Ager, Reference materials for calibrating magnetic permeability measuring equipment, IEEE Trans. Magn. 26 (5) (1990) 2050–2051.
[22] P. Arpaia, A. Liccardo, M. Buzio, A. Parrella, On the use of fluxmetric methods for characterizing feebly magnetic materials, in: 2017 IEEE International Instrumentation and Measurement Technology Conference (I2MTC), 2017, pp. 1–6.
[23] Z. Wang, T.A. Palmer, A.M. Beese, Effect of processing parameters on microstructure and tensile properties of austenitic stainless steel 304L made by directed energy deposition additive manufacturing, Acta Mater. 110 (2016) 226–235.
[24] J.D. Jackson, Classical Electrodynamics, John Wiley & Sons, 2007.
[25] B. Hao, K.-M. Lee, K. Bai, Eddy-current dynamic model for simultaneous geometrical and material parameter measurements of magnetic materials, in: ASME 2018 Dynamic Systems and Control Conference, 2018, V002T24A009.
[26] K. Fujiwara, T. Nakata, Results for benchmark problem 7 (asymmetrical conductor with a hole), Compel 9 (3) (1990) 137–154.
[27] C.R. Vogel, Computational Methods for Inverse Problems, vol. 23, SIAM, 2002.
[28] P.C. Hansen, Regtools, http://www2.compute.dtu.dk/~pcha/Regutools/, 2015, MATLAB Central File Exchange.